

2019

Conformational Flexibility in the Enterovirus RNA Replication Platform

Meghan S. Warden
Old Dominion University, mbrow160@odu.edu

Kai Cai
University of Wisconsin-Madison


Gabriel Cornilescu
University of Wisconsin-Madison

Jordan E. Burke
University of Wisconsin-Madison

Komala Ponniah
Old Dominion University, kponniah@odu.edu

See next page for additional authors

Follow this and additional works at: https://digitalcommons.odu.edu/chemistry_fac_pubs

 Part of the [Genetics and Genomics Commons](#), [Organic Chemistry Commons](#), [Virus Diseases Commons](#), and the [Viruses Commons](#)

Original Publication Citation

Warden, M. S., Cai, K., Cornilescu, G., Burke, J. E., Ponniah, K., Butcher, S. E., & Pascal, S. M. (2019). Conformational flexibility in the enterovirus RNA replication platform. *RNA*, 25(3), 376-387. <https://doi.org/10.1261/rna.069476.118>

This Article is brought to you for free and open access by the Chemistry & Biochemistry at ODU Digital Commons. It has been accepted for inclusion in Chemistry & Biochemistry Faculty Publications by an authorized administrator of ODU Digital Commons. For more information, please contact digitalcommons@odu.edu.

Authors

Meghan S. Warden, Kai Cai, Gabriel Cornilescu, Jordan E. Burke, Komala Ponniah, Samuel E. Butcher, and Steven M. Pascal

Conformational flexibility in the enterovirus RNA replication platform

MEGHAN S. WARDEN,¹ KAI CAI,² GABRIEL CORNILESCU,³ JORDAN E. BURKE,^{2,4} KOMALA PONNIAH,¹ SAMUEL E. BUTCHER,² and STEVEN M. PASCAL¹

¹Department of Chemistry and Biochemistry, Old Dominion University, Norfolk, Virginia 23529, USA

²Department of Biochemistry, University of Wisconsin-Madison, Madison, Wisconsin 53706, USA

³National Magnetic Resonance Facility at Madison (NMRFAM), University of Wisconsin-Madison, Madison, Wisconsin 53706, USA

ABSTRACT

A presumed RNA cloverleaf (5'CL), located at the 5'-most end of the noncoding region of the enterovirus genome, is the primary established site for initiation of genomic replication. Stem-loop B (SLB) and stem-loop D (SLD), the two largest stem-loops within the 5'CL, serve as recognition sites for protein interactions that are essential for replication. Here we present the solution structure of rhinovirus serotype 14 5'CL using a combination of nuclear magnetic resonance spectroscopy and small-angle X-ray scattering. In the absence of magnesium, the structure adopts an open, somewhat extended conformation. In the presence of magnesium, the structure compacts, bringing SLB and SLD into close contact, a geometry that creates an extensive accessible major groove surface, and permits interaction between the proteins that target each stem-loop.

Keywords: RNA; enterovirus; replication; NMR; SAXS; cloverleaf

INTRODUCTION

Enteroviruses are responsible for a number of diseases and conditions ranging from poliomyelitis to the common cold (Greenberg 2003). Their genetic information is carried as a small single-stranded RNA molecule (~7.5–8.3 kb) that is replicated through a highly conserved mechanism (Goodfellow et al. 2003). The genome consists of three distinct sections: an extensive 5' noncoding region (NCR) and a much smaller 3'-NCR, that together flank a large single open reading frame. This open reading frame encodes a single large polyprotein (~250 kDa). After translation, the polyprotein is systematically cleaved into a dozen or so structural and nonstructural proteins by virus-encoded proteases that are part of the polyprotein. The 3C protease is responsible for most of the cleavage events. In addition, a population of the 3C protease molecules remain covalently joined to the virus-encoded RNA-dependent RNA polymerase (3D), forming the fusion protein 3CD. The 3CD protein interacts directly with the 5'-NCR as an essential step in the replication process (Andino et al. 1990; Jacobson et al. 1993; Agol et al. 1999; Goodfellow et al. 2000).

The 5'-NCR can be further subdivided into two regions. A large (~400–500 bases) internal ribosome entry site

(IRES) is immediately 5' to the ORF, where it directs translation of the polyprotein without the need for a capped mRNA structure. At the extreme 5'-end of the genomic RNA, a smaller (~83 base) region, predicted to form a cloverleaf structure (5'CL) in enteroviruses, serves as the main replication platform for virus replication (Rivera et al. 1988; Pilipenko et al. 1989; Le and Zuker 1990; Gamarnik and Andino 1997). Sequence analysis of the 5'CL predicts the presence of one stem (stem A or SA) and three stem-loops (SLB, SLC, and SLD) (see Fig. 1). SLD attracts the fusion protein 3CD, delivering the 3D polymerase to the required site to begin synthesis of a negative strand RNA (Andino et al. 1990). This negative strand then serves as a template to produce multiple copies of the positive strand, which can be used as either additional mRNA or genetic material for nascent viral particles that are released from the cell and can go on to infect other cells.

The loop region of SLB contains a C-rich sequence that attracts the host poly(C)-binding protein (PCBP). PCBP functions both in translation, via binding to C-rich regions in the IRES, and in replication, via binding to the 5'CL SLB (Gamarnik and Andino 1997; Parsley et al. 1997). However, when PCBP is attached to the IRES, PCBP can be cleaved

⁴**Present address:** Department of Biochemistry and Biophysics, University of California-San Francisco, San Francisco, California 94143, USA

Corresponding author: spascal@odu.edu

Article is online at <http://www.majournal.org/cgi/doi/10.1261/rna.069476.118>.

© 2019 Warden et al. This article is distributed exclusively by the RNA Society for the first 12 months after the full-issue publication date (see <http://majournal.cshlp.org/site/misc/terms.xhtml>). After 12 months, it is available under a Creative Commons License (Attribution-NonCommercial 4.0 International), as described at <http://creativecommons.org/licenses/by-nc/4.0/>.

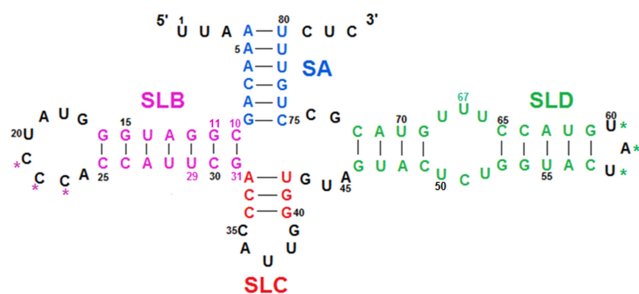


FIGURE 1. Secondary structure prediction of RV-B14 5'CL. The RV-B14 5'CL is predicted to form a four helix junction containing stem A (SA; blue), stem-loop B (SLB; magenta), stem-loop C (SLC; red), and stem-loop D (SLD; green). Protein binding sites in SLB (magenta stars) and SLD (green stars) are shown, along with colored numbering for key nucleotides discussed in the text.

by the virus-encoded 3C protease. The cleaved PCBP can then only function in replication. Thus, cleavage of IRES-bound PCBP serves effectively as a switching mechanism from translation to replication (Andino et al. 1990, 1993; Blyn et al. 1996, 1997; Barton et al. 2001). Furthermore, the binding of PCBP to SLB facilitates the binding of 3CD to SLD and triggers circularization of the RNA genome, two events that are essential for the synthesis of the negative strand (Gamarnik and Andino 1998). A better understanding of the structural basis of these interactions and their interdependence could lead to ways to inhibit virus replication, leading to effective treatment or immunization against the large number of diseases and conditions associated with enterovirus infection.

In this study, a combined nuclear magnetic resonance (NMR) and small-angle X-ray scattering (SAXS) approach has been used to determine the solution structure of the 5'CL RNA from serotype 14 of the rhinovirus (RV-B14). Results show that the cloverleaf conformation, in particular its compactness, conformational stability, and relative orientation of the two largest stem-loops (SLB and SLD), is highly dependent upon the *absence* versus *presence* of magnesium. This study represents an important step in the process of building a high-resolution structural understanding of enterovirus replication.

RESULTS

NMR analysis of RV-B14 5'CL

Peak assignments

Imino protons, which are present only in guanine (G) and uracil (U) bases, are highly exchangeable with solvent protons. Therefore, the presence of the imino resonance implies protection, most notably via hydrogen bonding in a stable base pair. The absence of an imino resonance conversely suggests the absence of a stable hydrogen bond and is often indicative of presence in a dynamic loop or

bulge region. Resonances of imino protons in a Watson–Crick base pair range from ~11.5–13 ppm (G) and ~13–15 ppm (U). Resonances observed outside of the above spectral range indicate the presence of a non-Watson–Crick base pair, such as a GU (10–12 ppm) or a UU base pair (10.4–11.3 ppm).

The RV-B14 5'CL molecule contains a total of 45 imino protons, 26 of which were observed in the two-dimensional $^1\text{H}, ^1\text{H}$ -NOESY spectrum (Fig. 2) in the *absence* of magnesium. Five strong resonances are located outside the spectral range of a Watson–Crick base pair and were assigned to nucleotides U50, U52, U66, U68, and G12 as described below. In general, imino proton resonances were assigned based on sequential imino–imino NOESY cross-peaks (Fig. 2), with the assistance of imino proton resonance assignments from previously published works with isolated RV-B14 SLB (Warden et al. 2017) and SLD (Headey et al. 2007). The observed pattern of sequential imino–imino NOE cross-peaks confirmed the formation of SA, SLB, SLC, and SLD helices, and the absence of additional imino resonances indicated nucleotides that are not involved in stable hydrogen bonding (for a full list of the hydrogen bond constraints, see Materials and Methods).

Chemical shift changes upon incorporation into cloverleaf

The imino chemical shift difference between SLB and SLD in previously described isolated stem-loops (Headey et al. 2007; Warden et al. 2017) versus when incorporated into the 5'CL (without magnesium) are shown in Figure 3A. The differences are small (RMSD 0.028 ppm),

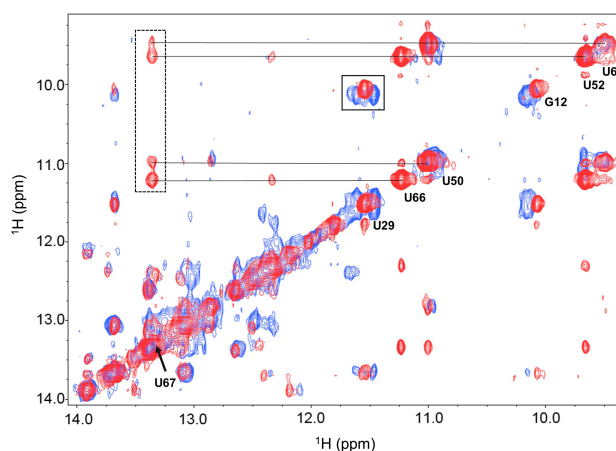


FIGURE 2. 2D $^1\text{H}, ^1\text{H}$ -NOESY of RV-B14 5'CL. Imino NOESY spectra in the absence (blue) and presence (red) of magnesium. The multiple resonances for nucleotide U29 in the absence of magnesium (solid box) collapse to a single resonance in the presence of magnesium. The imino resonance of nucleotide U67 is only observed upon the addition of magnesium, with sequential imino–imino cross-peaks to U67 shown in the dashed box.

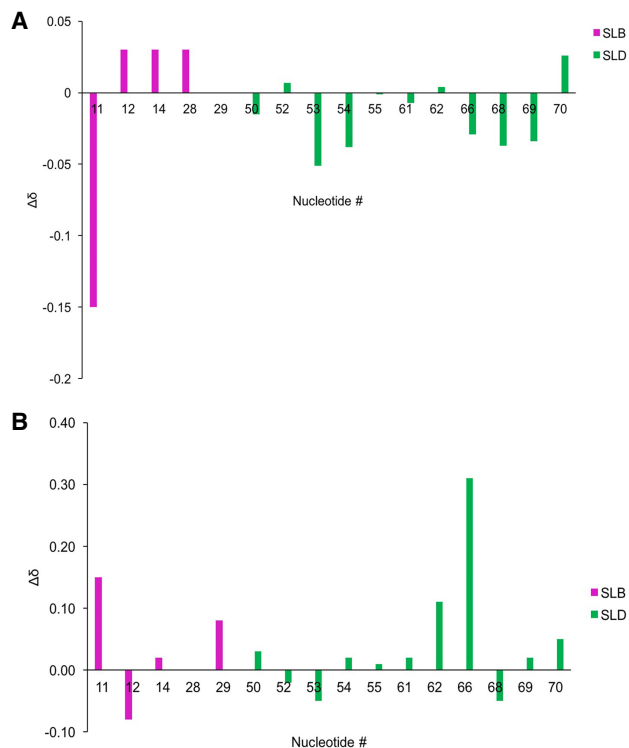


FIGURE 3. Chemical shift differences for RV-B14 5'CL. ^1H chemical shift changes within SLB (magenta) and within SLD (green) induced by incorporation into the 5'CL (A) in the absence of magnesium and (B) in the presence of magnesium.

consistent with conservation of the structure, excluding the large difference observed for G11. Also, a new peak appears for the G31 imino resonance, indicating stabilization of the C10–G31 base pair only in the 5'CL, and not in the isolated SLB. This effectively extends SLB by one base pair, matching the predicted length of SLB (see Fig. 1). This additional base pair evidently alters the chemical shift of the adjacent G11 resonance. In addition, the imino resonance of U29 appears to split into two or more resonances in the cloverleaf (Fig. 2), suggesting the presence of two or more slowly interconverting states, which was not observed in the isolated SLB structure. Since U29, G11, and G31 are from sequential base pairs at the junction end of SLB, it appears that alterations are localized to this region. To incorporate these data into 5'CL structure calculations in the *absence* of magnesium, hydrogen bonding constraints were added for C10–G31, and hydrogen bonding constraints were retained for G12–U29, but rigidity of the G12–U29 base pair was relaxed.

Chemical shift changes upon addition of magnesium

Upon addition of magnesium to the 5'CL, chemical shift changes indicate a return of SLB to its structure when isolated: the splitting of the U29 resonance disappears, the G31 imino resonance also disappears, and the G11

imino resonance returns to the chemical shift observed in the isolated SLB. Therefore, the above adjustments made to SLB for calculations in the *absence* of magnesium, were removed for calculations in the *presence* of magnesium.

Also, two significant changes are observed in SLD. First, a resonance appears for U67, indicating stabilization of the C51–U67 base pair from the pyrimidine mismatch region of SLD. Although the U67 imino resonance was not observed in the isolated SLD structure analysis (Headey et al. 2007), other NOEs and RDCs clearly indicated the presence of C51–U67 hydrogen bonding in isolated SLD, and so no change was required in the calculations, other than incorporation of the U67 imino RDC.

The second significant change in SLD is alteration of the U66 imino chemical shift by ~ 0.3 ppm (Fig. 3B). This alteration at the U52–U66 base pair is likely related to the above-mentioned stabilization of the adjacent C51–U67 base pair. This change is also related to a required adjustment made in calculations: In initial calculations of the 5'CL structure, both in the *presence* and in the *absence* of magnesium, both the U52 and U66 imino RDCs were consistently violated. Non-Watson–Crick base pairs containing two imino protons, such as U–U or G–U pairs, would be expected to have similar ^1H - ^{15}N RDC values if the base pair is nearly planar. However, the RDC values for the U52–U66 base pair were measured as 38.5 Hz for U52 and 16.3 Hz for U66 in the *absence* of magnesium, and 39.8 Hz for U52 and 32.8 Hz for U66 in the *presence* of magnesium. In the isolated structure of RV-B14 SLD, the imino bonds for U52 and U66 are nearly coplanar. Therefore, the conformation of the U52–U66 base pair in the 5'CL is not consistent with the isolated SLD structure. Therefore, for calculations in both the *absence* and *presence* of magnesium, hydrogen bonding constraints were retained for U52–U66, but rigidity of the base pair was relaxed, allowing the structure to adjust to the observed RDCs.

SAXS: global structure of RV-B14 5'CL

Small angle X-ray scattering (SAXS) probes the global shape of biological macromolecules in solution. SAXS is highly complementary to NMR: It is a mid-resolution technique that does not require crystallization or isotope labeling, has no size limitations, and requires low sample quantities. Here, SAXS was used to investigate the global structure of RV-B14 5'CL in the *absence* and *presence* of magnesium. The measured radius of gyration (R_g) and the maximum dimension (D_{max}) for the RV-B14 5'CL in the *absence* of magnesium were 26.8 and 85 Å, respectively. Upon the addition of 5 mM MgCl_2 , the R_g and D_{max} decreased to 22.3 and 70 Å, indicating that magnesium triggers a conformational change to a more compact structure, consistent with the NMR results discussed

above. A Kratky plot (q vs. $q^2 \bullet I$) can be used to assess the overall shape and flexibility of the molecule (Kikhney and Svergun 2015). A bell-shaped Kratky curve indicates a well-folded globular and compact conformation. The Kratky curves in the *presence* and *absence* of magnesium are shown in Figure 4A. The RV-B14 5'CL in the *absence* of magnesium shows a bell-curved shape with a slight plateau at higher q values, whereas the 5'CL in the *presence* of magnesium displays a more evenly distributed plot. This confirms that upon the addition of magnesium the 5'CL forms a more well-folded compact conformation. This more compact shape with the *presence* of magnesium is consistent with the pairwise distribution function [$P(r)$] plot in Figure 4B.

Full structural calculation: NMR and SAXS

In the *absence* of magnesium, 100 three-dimensional structures of RV-B14 5'CL were calculated as described in Materials and Methods, using simulated annealing and rigid body protocol as used by XPLOR-NIH (Schwieters et al. 2003). The eight best final structures selected to represent the conformation have an average pairwise RMSD of 7.735 Å with the A-form helix regions having an RMSD of 6.981 Å (Table 1; Fig. 5A). A similar procedure was performed on RV-B14 5'CL in the *presence* of 25 mM $MgCl_2$ with the eight lowest energy structures having an RMSD of 1.812 Å, and the A-form helical regions having an RMSD of 1.536 Å (Table 1; Fig. 5B). In the *absence* of mag-

nesium, 5'CL adopts an open conformation with SLB and SLD positioned $\sim 90^\circ$ apart. In the *presence* of magnesium, a more compact structure forms with SLB and SLD in close contact and arranged in a parallel form. The positions of SA and SLC in both structures are less defined, at least in part due to the short length of the helices, which renders their position less sensitive to fitting of both the NMR and SAXS data.

Comparison of SAXS-only models with SAXS/NMR-based structures

Medium-resolution ab initio models of the 5'CL shape (Fig. 4C), based only on the SAXS experimental profile, were calculated independently from the XPLOR-calculated structures, using DAMMIF software (Franke and Svergun 2009). In the *absence* of magnesium, the ab initio model is somewhat Λ -shaped, but with one leg longer than the other. Overlay of this model with the lowest energy SAXS/NMR-based structure from XPLOR-NIH calculations shows a good fit (χ^2 value of 1.44). The extended leg fits the longest stem-loop (SLD), while the next longest stem-loop, SLB, is fitted into the shorter leg. In this overlay, part of the SLB loop region extends outside of the ab initio model. However, this SLB loop has been shown to be highly dynamic (Warden et al. 2017), and so its position in this figure is somewhat misleading. As a dynamic loop, it can explore many conformations and positions, and so may not give rise to intense density in the ab initio model.

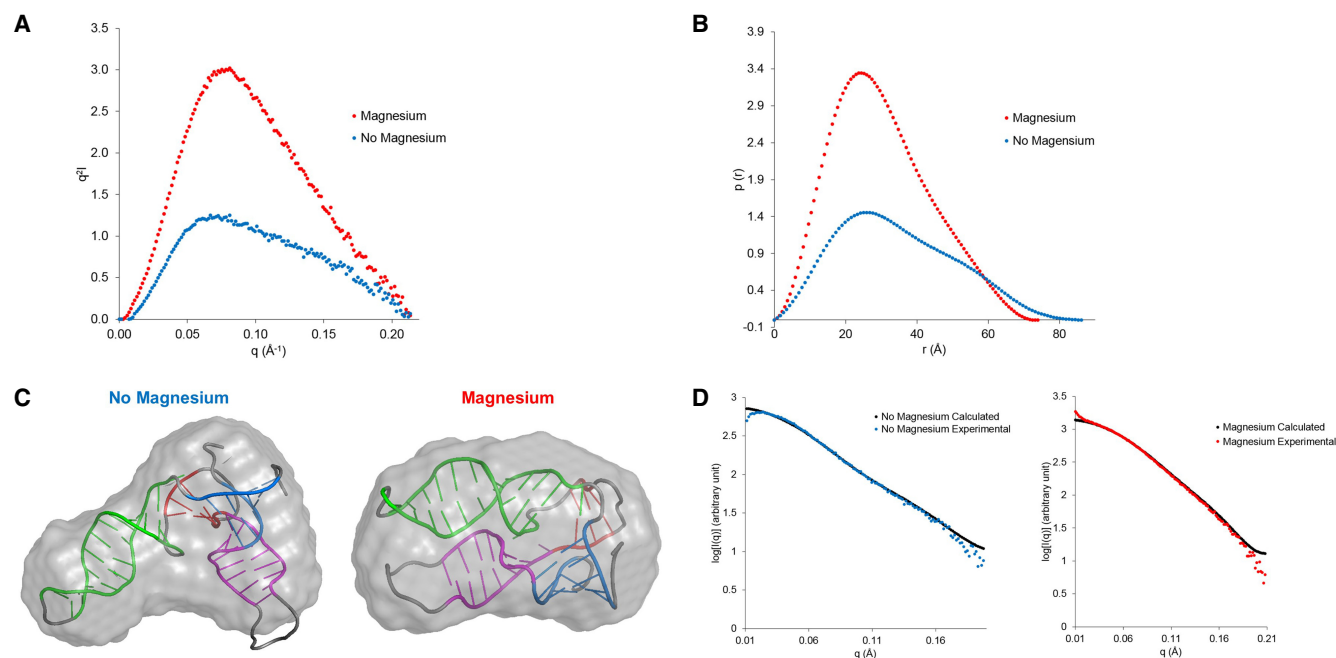


FIGURE 4. SAXS data plots for RV-B14 5'CL. Plots are shown for data in the absence (blue) and presence (red) of magnesium. (A) Kratky plot. (B) Pairwise distance distribution function. (C) SAXS-only ab initio models (gray surface) of 5'CL in the absence (*left*) and presence (*right*) of magnesium, overlaid with SAXS/NMR-based structures with the helices colored as shown in Figure 1. (D) Overlay of experimental and calculated SAXS profiles.

TABLE 1. Structural statistics for RV-B14 5'CL

RMS constraint/geometry violations	No magnesium	Magnesium
Pf1 RDCs (Hz)	0.923 ± 0.309	1.376 ± 0.113
SAXS data fit (χ^2)	1.440 ± 0.002	0.924 ± 0.001
Bond lengths (Å)	0.005 ± 0.001	0.004 ± 0.000
Bond angles (°)	0.673 ± 0.048	0.628 ± 0.008
Impropers (°)	0.382 ± 0.026	0.380 ± 0.024
Ensemble RMSD (Å)		
Stems	6.981	1.536
SLB and SLD	5.772	0.982
All atoms	7.735	1.812

In the *presence* of magnesium, the *ab initio* SAXS structure is more symmetrical and compact. This matches well with the XPLOR-NIH calculated structure in the *presence* of magnesium (χ^2 value of 0.924). The compactness arises when SLB and SLD align and come in to contact with each other. Together, these comparisons of *ab initio* SAXS-based models with the XPLOR models provide confirmation of structural veracity. Superimposition of the eight lowest energy structures and the SAXS *ab initio* model is shown in Supplemental Figure S2.

RNA four-way junction: helical arrangement

RNA junctions are common structural elements found in, for instance, ribosomes, ribozymes, group II introns, and tRNAs. The topology of a junction is characterized by the pattern of coaxial stacking of helices; pairs of helices interacting end-to-end to form one continuous or nearly continuous helix. Based on coaxial stacking patterns, RNA four-way junctions such as 5'CL (with four helices from SA, SLB, SLC, and SLD) can be classified into nine different families: families H, cH, and cL contain two pairs of coaxial helices; cK and π families contain one stacked helix pair each; cW, ψ , X, and cX families contain no stacked helices (Laing and Schlick 2009). The RV-B14 5'CL structure in the *absence* of magnesium shows no clear evidence of coaxial stacking for three of the eight final structures whereas the remaining five present possible stacking between helices SA and SLB.

Doubling present in $^1\text{H}, ^1\text{H}$ -NOESY spectrum, the longer axis length observed in the SAXS *ab initio* model and the $P(r)$ curve, and the decrease in intensity for the Kratky plot each support the notion that the structure in the *absence* of magnesium is somewhat extended (not maximally compact). Topologically, the structures fit either the cK or cX classification.

In the *presence* of magnesium, possible stacking of SA and SLB was also seen in two of the eight final structures, with no stacking evident in the remaining structures. Although somewhat similar coaxial stacking patterns are observed for both conditions, in the *presence* of magnesium the structure topology is very different, with more evidence of ordered compactness, and with the two longest stems, SLB and SLD, positioned parallel to each other and in close association. Topologically, most of the structures fit the cW or ψ classification.

DISCUSSION

Enterovirus replication is a highly conserved mechanism that is initiated by protein–RNA complexes forming upon the 5'CL RNA. A C-rich region of the SLB loop specifically

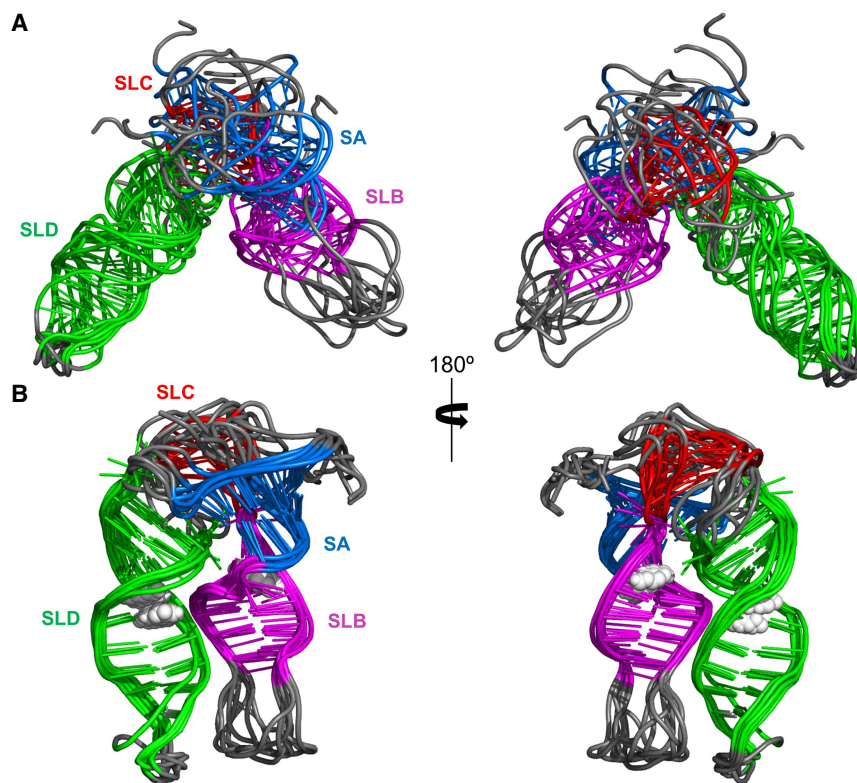


FIGURE 5. Structure of RV-B14 5'CL. Superimposition of the eight lowest energy structures of RV-B14 5'CL in (A) the absence of magnesium and (B) the presence of magnesium. The loop and terminal regions are colored in gray, the stem regions are colored as in Figure 1. Atoms from the bases of U29, U66, and U67, each of which show significant changes in NMR spectra upon addition of magnesium, are shown as white spheres.

binds to the host poly(C)-binding protein (PCBP), facilitating the binding of virus fusion protein 3CD with SLD (Gamarnik and Andino 1998). The PCBP then coordinates with the host poly(A)-binding proteins (PABP) that binds to the A-rich 3'UTR in the virus genome (Barton et al. 2001; Herold and Andino 2001). The PCBP–PABP interaction effectively circularizes the virus genomic RNA, allowing the RNA replicase (3D) to access the 3'-UTR, where negative strand synthesis initiates. Thus, circularization requires protein–RNA interactions by PCBP, PABP, and 3CD (Gamarnik and Andino 1997; Parsley et al. 1997). The resulting nascent negative strand is then used as a template to create a large number of new positive RNA strands that serve as mRNA and as genetic material for new virus particles. The determination of the three-dimensional structure of RV-B14 5'CL, particularly the relative position and orientation of SLB and SLD, upon which PCBP and 3CD assemble, is a vital step toward understanding the replication mechanism of enteroviruses and toward developing therapeutic agents for inhibition of enterovirus replication.

Influence of magnesium

The present study presents two distinct structures for RV-B14 5'CL, in the *absence and presence* of magnesium (Fig. 5). Metal cations play a vital role in RNA folding and stabilization in many biological processes. The positive charge of metal cations can shield the repulsion of the phosphate ions present in the backbone of RNA, allowing RNA to fold into a more stable and compact tertiary conformation. Magnesium is the most often identified cation in RNA structures and is considered the most important divalent cation for RNA stabilization (Tinoco and Bustamante 1999; Gonzalez and Tinoco 2001; Woodson 2005).

In the *absence* of magnesium, RV-B14 5'CL takes on an open conformation with SLB and SLD approximately perpendicular to one another (Fig. 5A). As discussed in the Results section, some structural dynamics is suggested by relatively broad NMR line shapes, doubling of some imino resonances in the ^1H , ^1H -NOESY spectrum and a relatively low intensity in the Kratky plot and $P(r)$ curve (Fig. 4). In contrast, in the *presence* of magnesium, SLB and SLD move toward each other to form a more compact and more ordered structure (Fig. 5B). Close association of the stems from SLB and SLD results in positioning of the two corresponding loop regions in close proximity (Fig. 5B).

The magnesium-induced association of SLB and SLD suggests that

magnesium binds somewhere along the SLB/SLD interface, helping to screen charge–charge repulsions between the phosphodiester backbones of the two stems. Consistent with this hypothesis, the largest NMR spectral changes in chemical shift upon addition of magnesium (Fig. 3B) occur at nucleotides 11, 12, 29, 62, and 66, each of which are in SLB or SLD. In addition, as discussed previously, doubling of the U29 resonance disappears and a new peak arises for the U67 imino resonance.

The observed chemical shift changes seen at bases 11 and 12 upon magnesium addition are related to the destabilization of base pair C10–G31 as discussed in the Results section. The remaining large changes occur in bases 29, 62, 66, and 67. Three of these bases, U29, U66, and U67, come into close contact with each other in the magnesium structure (Fig. 5B, depicted as spheres). This suggests stable site binding of magnesium very near these three bases.

Fold in absence of magnesium

Closer examination of the structures in the *absence* of magnesium reveals the presence of two distinct structural subgroups, differing in the orientation of SA relative to SLB. The first subgroup contains five of the eight structures (Fig. 6A) with the orientation of SA to SLB similar to the relative orientation in the *presence* of magnesium (Fig. 6B). The remaining three structures effectively reverse the positions of SA and SLC, with SA appearing behind SLC in this view (see Supplemental Fig. S1). Both subgroups fit the NMR and SAXS data, however, the first subgroup (Fig. 6A) has somewhat lower calculated energy, and would require far less structural rearrangement to form the closed structure upon addition of magnesium. The first subgroup shows stacking of SA and SLB, while the second subgroup

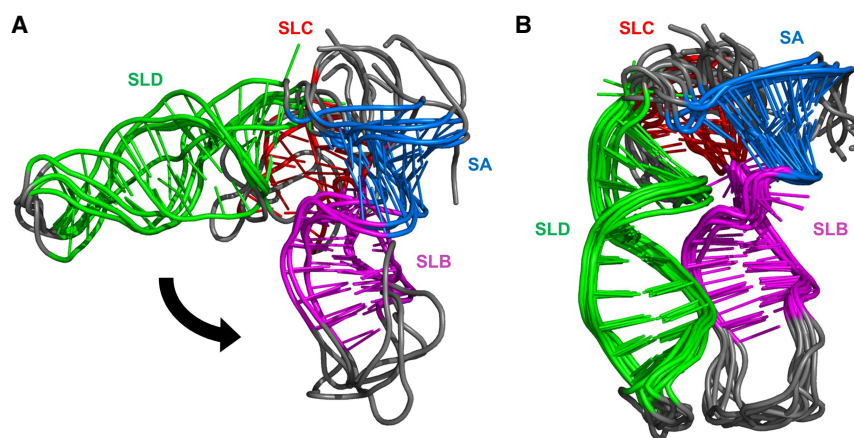


FIGURE 6. Changes in orientation induced by magnesium. (A) Structure in the absence of magnesium. (B) Structure in the presence of magnesium. The black arrow in part A illustrates the change in position of SLD due to the addition of magnesium. Stem regions are colored as in Figure 1.

does not. Topologically, the junction classification of subgroup 1 is cK, while the classification of subgroup 2 is cX. The above evidence suggests that the cK structure is the correct fold in the *absence* of magnesium.

The SAXS/NMR approach

The combined SAXS/NMR analysis of RNA structure is by now a relatively well-established technique (e.g., Grishaev et al. 2008; Burke et al. 2012; Cornilescu et al. 2016; for recent review, see Mertens and Svergun 2017). Furthermore, when high-resolution structures of the isolated stem-loops are available (via conventional NMR or crystallographic analyses), and when the conservation of these separate structures is verified upon incorporation into the complex, the SAXS/NMR approach is capable of producing high-resolution information. In the present case, prior high-resolution structures are available for the largest two stem-loops (SLB and SLD [Headey et al. 2007; Warden et al. 2017]); which together comprise 61% of the total cloverleaf. As discussed in the Results section, chemical shift analysis, together with RDC and SAXS fitting, confirm that SLB and SLD structures are largely conserved upon incorporation into the cloverleaf, and pertinent measures were taken to adjust the individual structures to the few data that indicate localized rearrangement.

Information regarding the relative positioning of SLB versus SLD in the cloverleaf is obtained via a combination of orientational information for each helix from RDC analysis and global shape information from SAXS analysis. The combined result is unambiguous: SLB and SLD are oriented well apart from one another, nearly at a right angle, in the *absence* of magnesium, while they come together to interact closely in the *presence* of magnesium.

SLB and SLD major grooves and relative helical twist

Typical A-form RNA contains a narrow (2.4 Å width) but deep major groove and a wide but shallow minor groove. The narrow major groove restricts protein access for base-specific interactions to the minor groove side. However, the isolated solution structures of RV-B14 SLB and SLD each contain atypically wide and accessible major grooves (9 Å and 13 Å width, respectively) (Headey et al. 2007; Warden et al. 2017), a feature that is retained upon incorporation into the cloverleaf (see below). In this context, it is interesting to note that magnesium has been shown to help stabilize non-Watson-Crick base pairs (Correll et al. 1997).

The observed accessibility of the SLB major groove is simply due to the brevity of the SLB helix (6–7 base pairs): It contains too few base pairs to form a complete turn (11

base pairs) in order to close off the major groove. The characteristics of SLB are not otherwise unusual.

The SLD helix, on the other hand, contains 12 base pairs when the three central U–U and U–C pairs are included. This length would be sufficient to close off the major groove if the structure was standard A-form. However, the presence of the non-Watson-Crick pyrimidine mismatch regions in the center of SLD appears to disrupt standard A-form geometry. Non-Watson-Crick base pairs have been shown to induce widened major grooves that serve as recognition sites for protein–RNA interactions (Tanaka et al. 1999; Simon et al. 2015) for instance in the HIV RRE/Rev peptide interaction (Battiste et al. 1996). This can be understood by noting that base-pairing of two pyrimidines requires closer inter-helical approach than does a Watson-Crick pyrimidine–purine base pair, a stress which must distort the helix (same refs as above). Similar widening of the major groove was also reported for SLD from Coxsackievirus B3 (Ohlenschläger et al. 2004) and for a consensus enterovirus SLD sequence (Du et al. 2004).

We find no evidence that this established characteristic of SLD is lost when incorporated into the 5'CL. As an additional test, we computationally replaced the three central pyrimidine–pyrimidine base pairs in SLD with Watson-Crick pairs, and created a standard A-form SLD computational mutant. Using the same XPLOR-NIH routine, we were unable to find an orientation of the mutant SLD that fits the observed H–N RDCs (removing RDCs from the mismatch region). This, together with the contrasting ability to fit all data using the previously determined SLD structure, with modification only of one U–U base pair orientation as described in the Results section, corroborates that the SLD structure is largely conserved in the cloverleaf.

Next, we analyzed the relative positions of the SLB and SLD accessible major grooves, in the *presence* of magnesium. The ability of the SAXS/NMR approach to determine the relative helical twist of stem-loops has been previously reported (e.g., Grishaev et al. 2008; Burke et al. 2012). In the present case, the relative helical twist of SLB and SLD orients the two accessible major groove regions in alignment with each other, creating a single accessible groove surface (Fig. 7). This surface is ~30 Å in length, and spans the width of the cloverleaf. Access to this groove surface could potentially stabilize interactions with host and virus proteins during replication, suggesting that it may prove to be an attractive therapeutic target.

Protein–RNA modeling

In order to begin to understand how the replication complex forms, interactions of the 5'CL with the virus 3C protein and the host PCBP KH1 domain were modeled (Fig. 8). Modeling was based on the previously determined solution structure of isolated RV-B14 SLD complexed with 3C

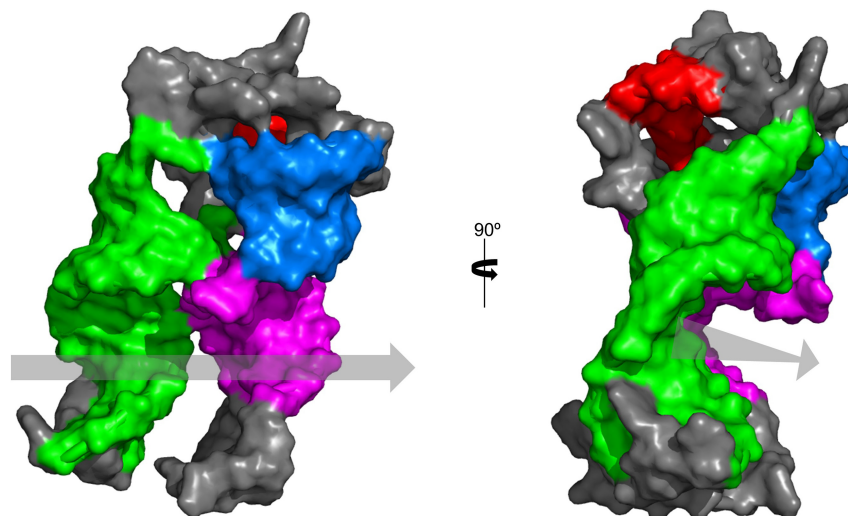


FIGURE 7. Major groove accessibility within RV-B14 5'CL. SLB and SLD from RV-B14 each contain accessible major groove regions, which align in the presence of magnesium. The gray arrow illustrates the position of the combined/aligned major groove in two different views of the structure in the presence of magnesium. Stem regions are colored as in Figure 1.

(Claridge et al. 2009), and a previously determined structure of the KH1 domain of PCBP with an oligonucleotide of sequence AACCCCTA, which is similar to the sequence in the 5'CL SLB C-rich loop (Du et al. 2005). The model in Figure 9 is based on previously determined structure of the poliovirus 3CD fusion protein (Marcotte et al. 2007). In Figure 9, 3D polymerase is positioned in front of the accessible groove. The 3D protein, fused to the 3C protein that binds SLD, is also positioned near the KH1 domain of PCBP that interacts with the SLB loop region.

The ability of magnesium to alter the 5'CL structure provides evidence that the two structures presented here, the open and closed conformation, could perhaps each be present during different steps in the replication cycle, under the appropriate conditions. Ionic environment, and also other factors, such as protein interactions, may tip this conformational balance. For instance, it is possible that the closed conformation binds PCBP and 3CD, but then circularization via interaction of PCBP with PABP may cause or require a switch to the open conformation. Such a switch to the open conformation could in turn be required to correctly position 3D at the 3'NCR for initiation of negative strand synthesis. Further structural studies performed with the 5'CL and replication proteins will however be needed to establish the role, if any, of 5'CL conformational switching in the replication mechanism of enteroviruses.

MATERIALS AND METHODS

RNA preparation

A DNA transcription template was designed to contain a T7 RNA polymerase promoter followed by a 5' *cis*-acting hammerhead ribozyme sequence and 83 nucleotides corresponding to RV-B14 5'CL. The double-stranded DNA plasmid was cloned into the pUC19 vector using the EcoR1 and BamH1 restriction sites. For in vitro transcription, the DNA plasmid was linearized using Bsa1. A natural abundance RNA sample of RV-B14 5'CL was produced by in vitro transcription using T7 RNA polymerase (expressed and purified in house) with RNAPoly reaction buffer (New England Biolabs; 40 mM Tris-HCl, 6 mM MgCl₂, 10 mM DTT, and 2 mM spermidine, pH 7.9), each rNTP at 5 mM (Sigma), 0.02 mg/mL double-stranded DNA template, and 0.001 unit/mL pyrophosphatase (Fisher). A 10 mL transcription reaction mixture was incubated at 37°C for 3 h, and the RNA was ethanol precipitated with 2.5 volumes of 100% ethanol and 0.1 volumes of 3 M sodium acetate, and the mixture was incubated overnight at -20°C. The solution was spun down at 9200g, 4°C. The resulting pellet was washed in 70% ethanol and spun down for an additional 10 min at 9200g. The pellet was dissolved in 8 M urea loading buffer (8 M urea, 25 mM EDTA, 500 mM Tris-HCl, 4.6 mM xylene cyanol, and 3.7 mM bromophenol blue, pH 7.9) and heated for 3 min at 98°C prior to gel purification. The RNA was resolved on a 6% denaturing polyacrylamide gel containing 8 M urea and visualized via ultraviolet (UV) shadowing at 254 nm, and the corresponding band was excised from the gel. The RNA was recovered from the gel pieces using an Elutrap device (Whatman) in 1× Tris-borate-EDTA (TBE) buffer, pH 7.9. The concentration of the eluted RNA was determined

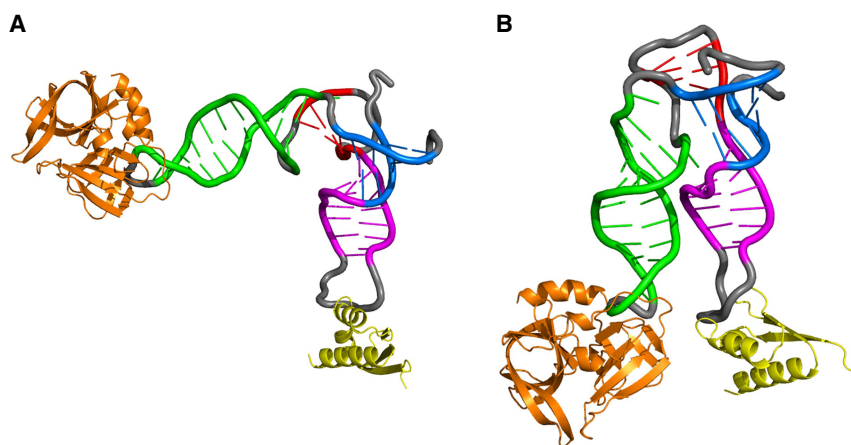


FIGURE 8. RNA-protein interaction modeling. Modeled binding of PCBP KH1 domain (yellow) with SLB and 3C protease (orange) with SLD (A) in the absence and (B) in the presence of magnesium. Stem regions are colored as in Figure 1.

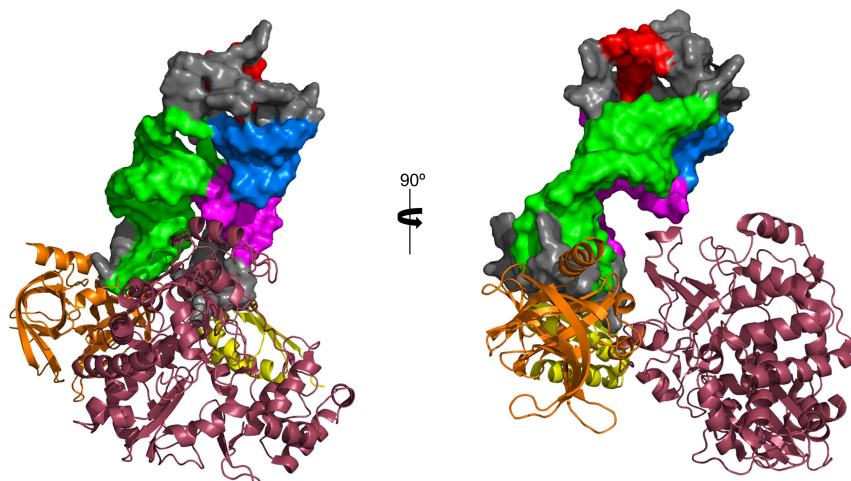


FIGURE 9. RNA–protein interaction modeling. Modeled binding of PCBP KH1 domain (yellow) with SLB and poliovirus 3CD protease (3C: orange, 3D: rose) with SLD, using the 5'CL structure in the presence of magnesium. Stem regions are colored as in Figure 1.

using a Biodrop UV-visible spectrophotometer. The RNA was concentrated and buffer exchanged using a Vivaspin spin concentrator (3 kDa cutoff) to a final concentration of 6 mg/mL in NMR buffer (10 mM sodium phosphate and 0.1 mM EDTA, pH 7.0). The sample was purified with Superdex 200 Increase 10/300 GL gel filtration column and further diluted to create 3 mg/mL and 1.5 mg/mL samples (SAXS samples). All three samples (6, 3, and 1.5 mg/mL) were dialyzed thoroughly with degassed NMR buffer. The dialysis buffer was retained for SAXS solvent blank measurements. An additional three samples (6, 3, and 1.5 mg/mL) were purified and dialyzed in NMR buffer containing 5 mM MgCl_2 . A labeled sample of the 5'CL was similarly produced using 2 mM each of ^{13}C and ^{15}N -labeled rGTP and rUTP (Cambridge Isotope Laboratories) with 8 mM each of natural abundance rATP and rCTP (Sigma). The sample was divided to produce one labeled sample with 25 mM MgCl_2 and one sample containing no MgCl_2 .

NMR spectroscopy

A 0.50 mM unlabeled RNA sample in 10 mM sodium phosphate and 0.1 mM EDTA (pH 7.15) containing 90% H_2O /10% D_2O mixture was used for the assignment of exchangeable protons. NMR experiments used for structure calculations were performed on a Bruker Avance-III 750 MHz at the National Magnetic Resonance Facility at Madison (NMRFAM) equipped with a cryoprobe. For assignment of exchangeable proton resonances, ^1H , ^1H -NOESY spectra in H_2O were recorded, in the *absence and presence* of 25 mM magnesium chloride, with mixing times of 150 msec at 5.1°C with 256 increments, 2048 data points, 160 scans per fid using excitation sculpting with gradients for water suppression.

Samples with uniform ^{13}C and ^{15}N enrichment of G and U nucleotides, in the *absence and presence* of 25 mM magnesium chloride, were used for residual dipolar coupling (RDC) measurements. ^1H , ^{15}N -ARTSY spectra were recorded in isotropic media, and in the presence of 12 mg/mL Pf1 filamentous bacteriophage. The error of the RDC measurement was assessed via the ratio of the isotropic and attenuated peak intensities compared to the

spectral noise (Ying et al. 2011). The data for all NMR spectra were processed using NMRPipe (Delaglio et al. 1995) and visualized and analyzed using NMRDraw and NMRViewJ (Norris et al. 2016).

Small-angle X-ray scattering

SAXS experiments were carried out on a Bruker Nanostar benchtop SAXS system (Bruker AXS) at NMRFAM equipped with a rotating anode (Cu) Turbo X-ray Source and a VÅNTEC-2000 (2048 × 2048 pixel) detector. Measurements were carried out in 10 mM NaP_i , 0.1 mM EDTA, pH 7.15 in the *absence and presence* of 5 mM MgCl_2 . The buffer used for the SAXS experiments contains 10 mM NaP_i and 0.1 mM EDTA, pH 7.15. Samples of 5'CL and 5'CL with magnesium were clarified by passage through a 0.2 mm filter before loading into a glass capillary cell. SAXS

data were collected at three concentrations 1.5, 3, and 6 mg/mL. No significant inter-particle interactions were observed for any of the concentrations. The 3 mg/mL data was used for model calculation. The sample-to-detector distance was set at ~ 1 m, allowing for the detection range: $0.012 > q > 0.25 \text{ \AA}^{-1}$. Forty microliters of RNA and buffer samples were loaded separately into a capillary cell with 1 mm diameter, and scattering data were collected for 4 h. The ATSAS software suite (Petoukhov et al. 2012) was used to process the SAXS data. The R_g for each sample was determined by using the Guinier approximation in the q range ($q_{\text{max}} \cdot R_g$) < 1.3 . Pairwise distance distribution functions [$P(r)$] were obtained using the GNOM software (Svergun 1992). The output from GNOM was then used in conjunction with DAMMIF (Franke and Svergun 2009) to generate 20 independent ab initio dummy atom models to assess the molecular shape of each sample. No symmetries were enforced during the calculations. Most of the models exhibited excellent agreement with experimental data and had a normalized spatial discrepancy (NSD) < 1 . CRYSOLOG software (Svergun et al. 1995) was used to compare the 5'CL structures with experimental SAXS data. Supcomb software (Kozin and Svergun 2001) was used to superimpose the 5'CL structures on to the SAXS ab initio dummy atom models. The V_c approach was used for the molecular weight calculation from the SAXS data (Rambo and Tainer 2013). The detailed data acquisition and analysis parameters are listed in Supplemental Table S1.

NMR/SAXS-based structure calculation and refinement

A total of 2000 preliminary structural models for RV-B14 5'CL were generated using MC-Sym (Parisien and Major 2008). The MC-Sym models were built using reference pdb files for each domain of the 5'CL, which consisted of the previously determined structures of RV-B14 SLB (Warden et al. 2017) and SLD (Huang et al. 2001; Headey et al. 2007; Claridge et al. 2009) together with SA and SLC structures generated using RNAComposer (Popenda et al. 2012), the latter two based on secondary structure prediction

and confirmed via assignment of imino proton peaks in the above ^1H , ^1H -NOESY spectra of the 5'CL. For the nonmagnesium data, the 2000 models were filtered down to 500 models by comparing 20 ^1H - ^{15}N experimental RDC versus calculated RDC values determined using PALES (Zweckstetter 2008). The 500 models were subject to χ^2 goodness-of-fit analysis between the experimental and the calculated SAXS profile, with the 10 structures having the lowest χ^2 values ($\chi^2 < 15.1$) taken as preliminary structures to begin XPLOR-NIH (Schwieters et al. 2003) calculations. The procedure was repeated for the data in the presence of magnesium, and 10 best structures with the lowest χ^2 value ($\chi^2 < 16.5$) were chosen for further refinement with XPLOR-NIH (Schwieters et al. 2003).

In the case of the nonmagnesium sample, for each of the 10 preliminary pDBs, 10 refined structural models were calculated using a simulated annealing and rigid body refinement protocol in XPLOR-NIH (Schwieters et al. 2003) that incorporated both the NMR and SAXS data with floating alignment tensor. In initial calculations in the absence of magnesium, the stem regions of the SA (A5:G9 and C75:U79), SLB (C10:G16 and C25:G31), SLC (A32:C34 and G40:U42) and SLD (U47:C57 and G61:A71) structures were held rigid and contained hydrogen bond constraints, while the nucleotides in the loop and junction regions were given torsional degrees of freedom along with two other nucleotides whose ^1H imino resonances were not visible in the 2D ^1H , ^1H -NOESY (G46 and U80). For final calculations, rigidity was removed for nucleotides U52, U66, G12, and U29; however, hydrogen bond constraints for these were retained, as described further in the Results section. In the presence of magnesium, based upon similar imino assignments and NOEs, the regions of the stem-loops held rigid were the same as the initial calculations above for the absence of magnesium, with the following exceptions: nucleotides U52, U66, C10, and G31. The hydrogen bond constraints were retained for U52 and U66, but were removed for C10 and G31, as described further in the Results section.

In simulated annealing calculations, the initial annealing temperature was set to 3000K with a final temperature of 25K. The force constants for hydrogen bond constraints were ramped from 2 to 50 kcal mol $^{-1}$ Å $^{-2}$ and from 0.02 to 5 kcal mol $^{-1}$ rad $^{-2}$ for RDC constraints. In the case of no magnesium, the structures were refined with 105 SAXS data points ($0.03 < q < 0.18$ Å $^{-1}$) using 20 one-bond ^1H - ^{15}N RDCs, 50 planarity constraints, 124 hydrogen bond-derived constraints along with SAXS data and rigid body minimization in XPLOR-NIH (Schwieters et al. 2003). From the resulting 100 total refined structures, the eight lowest energy structures found with no RDC violations greater than 3 Hz and SAXS χ^2 value of 1.44 or less were taken as the final ensemble, with a pairwise RMSD of 7.735 Å (Fig. 5A). Similarly, from the 100 refined structures in the presence of magnesium, eight structures were found with no RDC violations greater than 3 Hz and SAXS χ^2 value of 0.924 or less. These eight structures were taken as the final structural ensemble in the presence of magnesium, with an average pairwise RMSD of 1.812 Å. The constraint and geometry calculations for each condition are shown in Table 1.

SUPPLEMENTAL MATERIAL

Supplemental material is available for this article.

ACKNOWLEDGMENTS

We thank John Markley. This study made use of NMR and SAXS instruments at the National Magnetic Resonance Facility at Madison, which is supported by National Institutes of Health grant P41GM103399 (NIGMS). NMR equipment was purchased with funds from the University of Wisconsin-Madison; the National Institutes of Health (P41GM103399, S10RR02781, S10RR08438, S10RR023438, S10RR025062, and S10RR029220); the National Science Foundation (DMB-8415048, OIA-9977486, and BIR-9214394); the National Institutes of Health R35GM118131 to S.E.B.; and the United States Department of Agriculture. This work was supported by startup funds and Program for Undergraduate Research and Scholarship grants from Old Dominion University.

Received November 1, 2018; accepted December 19, 2018.

REFERENCES

- Agol VI, Paul AV, Wimmer E. 1999. Paradoxes of the replication of picornaviral genomes. *Virus Res* **62**: 129–147. doi:10.1016/S0168-1702(99)00037-4
- Andino R, Rieckhof GE, Baltimore D. 1990. A functional ribonucleoprotein complex forms around the 5' end of poliovirus RNA. *Cell* **63**: 369–380. doi:10.1016/0092-8674(90)90170-J
- Andino R, Rieckhof GE, Achacoso PL, Baltimore D. 1993. Poliovirus RNA synthesis utilizes an RNP complex formed around the 5' end of viral RNA. *EMBO J* **12**: 3587–3598. doi:10.1002/j.1460-2075.1993.tb06032.x
- Barton DJ, O'Donnell BJ, Flanagan JB. 2001. 5' cloverleaf in poliovirus RNA is a cis-acting replication element required for negative-strand synthesis. *EMBO J* **20**: 1439–1448. doi:10.1093/emboj/20.6.1439
- Battiste JL, Mao H, Rao NS, Tan R, Muhandiram DR, Kay LE, Frankel AD, Williamson JR. 1996. α helix-RNA major groove recognition in an HIV-1 rev peptide-RRE RNA complex. *Science* **273**: 1547–1551. doi:10.1126/science.273.5281.1547
- Blyn LB, Swiderek KM, Richards O, Stahl DC, Semler BL, Ehrenfeld E. 1996. Poly(rC) binding protein 2 binds to stem-loop IV of the poliovirus RNA 5' noncoding region: identification by automated liquid chromatography-tandem mass spectrometry. *Proc Natl Acad Sci* **93**: 11115–11120. doi:10.1073/pnas.93.20.11115
- Blyn LB, Towner JS, Semler BL, Ehrenfeld E. 1997. Requirement of poly(rC) binding protein 2 for translation of poliovirus RNA. *J Virol* **71**: 6243–6246.
- Burke JE, Sashital DG, Zuo X, Wang YX, Butcher SE. 2012. Structure of the yeast U2/U6 snRNA complex. *RNA* **18**: 673–683. doi:10.1261/rna.031138.111
- Claridge JK, Headey SJ, Chow JY, Schwalbe M, Edwards PJ, Jeffries CM, Venugopal H, Trewhella J, Pascal SM. 2009. A picornaviral loop-to-loop replication complex. *J Struct Biol* **166**: 251–262. doi:10.1016/j.jsb.2009.02.010
- Cornilescu G, Didychuk AL, Rodgers ML, Michael LA, Burke JE, Montemayor EJ, Hoskins AA, Butcher SE. 2016. Structural analysis of multi-helical RNAs by NMR-SAXS/WAXS: application to the U4/U6 di-snRNA. *J Mol Biol* **428**: 777–789. doi:10.1016/j.jmb.2015.11.026
- Correll CC, Freeborn B, Moore PB, Steitz TA. 1997. Metals, motifs, and recognition in the crystal structure of a 5S rRNA domain. *Cell* **91**: 705–712. doi:10.1016/S0092-8674(00)80457-2

- Delaglio F, Grzesiek S, Vuister GW, Zhu G, Pfeifer J, Bax A. 1995. NMRPipe: a multidimensional spectral processing system based on UNIX pipes. *J Biomol NMR* **6**: 277–293. doi:10.1007/BF00197809
- Du Z, Yu J, Ulyanov NB, Andino R, James TL. 2004. Solution structure of a consensus stem-loop D RNA domain that plays important roles in regulating translation and replication in enteroviruses and rhinoviruses. *Biochemistry* **43**: 11959–11972. doi:10.1021/bi048973p
- Du Z, Lee JK, Tjhen R, Li S, Pan H, Stroud RM, James TL. 2005. Crystal structure of the first KH domain of human poly(C)-binding protein-2 in complex with a C-rich strand of human telomeric DNA at 1.7 Å. *J Biol Chem* **280**: 38823–38830. doi:10.1074/jbc.M508183200
- Franke D, Svergun DI. 2009. DAMMIF, a program for rapid *ab-initio* shape determination in small-angle scattering. *J Appl Crystallogr* **42**: 342–346. doi:10.1107/S0021889809000338
- Gamarnik AV, Andino R. 1997. Two functional complexes formed by KH domain containing proteins with the 5' noncoding region of poliovirus RNA. *RNA* **3**: 882–892.
- Gamarnik AV, Andino R. 1998. Switch from translation to RNA replication in a positive-stranded RNA virus. *Genes Dev* **12**: 2293–2304. doi:10.1101/gad.12.15.2293
- Gonzalez RL Jr, Tinoco I Jr. 2001. Identification and characterization of metal ion binding sites in RNA. *Methods Enzymol* **338**: 421–443. doi:10.1016/S0076-6879(02)38231-4
- Goodfellow I, Chaudhry Y, Richardson A, Meredith J, Almond JW, Barclay W, Evans DJ. 2000. Identification of a *cis*-acting replication element within the poliovirus coding region. *J Virol* **74**: 4590–4600. doi:10.1128/JVI.74.10.4590-4600.2000
- Goodfellow IG, Kerrigan D, Evans DJ. 2003. Structure and function analysis of the poliovirus *cis*-acting replication element (CRE). *RNA* **9**: 124–137. doi:10.1261/ma.2950603
- Greenberg SB. 2003. Respiratory consequences of rhinovirus infection. *Arch Int Med* **163**: 278–284. doi:10.1001/archinte.163.3.278
- Grishaev A, Ying J, Canny MD, Pardi A, Bax A. 2008. Solution structure of tRNA^{Val} from refinement of homology model against residual dipolar coupling and SAXS data. *J Biomol NMR* **42**: 99–109. doi:10.1007/s10858-008-9267-x
- Headley SJ, Huang H, Claridge JK, Soares GA, Dutta K, Schwalbe M, Yang D, Pascal SM. 2007. NMR structure of stem-loop D from human rhinovirus-14. *RNA* **13**: 351–360. doi:10.1261/ma.313707
- Herold J, Andino R. 2001. Poliovirus RNA replication requires genome circularization through a protein-protein bridge. *Mol Cell* **7**: 581–591. doi:10.1016/S1097-2765(01)00205-2
- Huang H, Alexandrov A, Chen X, Barnes TW III, Zhang H, Dutta K, Pascal SM. 2001. Structure of an RNA hairpin from HRV-14. *Biochemistry* **40**: 8055–8064. doi:10.1021/bi010572b
- Jacobson SJ, Konings DA, Samow P. 1993. Biochemical and genetic evidence for a pseudoknot structure at the 3' terminus of the poliovirus RNA genome and its role in viral RNA amplification. *J Virol* **67**: 2961–2971.
- Kikhney AG, Svergun DI. 2015. A practical guide to small angle X-ray scattering (SAXS) of flexible and intrinsically disordered proteins. *FEBS Lett* **589**: 2570–2577. doi:10.1016/j.febslet.2015.08.027
- Kozin MB, Svergun DI. 2001. Automated matching of high- and low-resolution structural models. *J Appl Crystallogr* **34**: 33–41. doi:10.1107/S0021889800014126
- Laing C, Schlick T. 2009. Analysis of four-way junctions in RNA structures. *J Mol Biol* **390**: 547–559. doi:10.1016/j.jmb.2009.04.084
- Le SY, Zuker M. 1990. Common structures of the 5' non-coding RNA in enteroviruses and rhinoviruses: thermodynamical stability and statistical significance. *J Mol Biol* **216**: 729–741. doi:10.1016/0022-2836(90)90395-3
- Marcotte LL, Wass AB, Gohara DW, Pathak HB, Arnold JJ, Filman DJ, Cameron CE, Hogle JM. 2007. Crystal structure of poliovirus 3CD protein: virally encoded protease and precursor to the RNA-dependent RNA polymerase. *J Virol* **81**: 3583–3596. doi:10.1128/JVI.02306-06
- Mertens HDT, Svergun DI. 2017. Combining NMR and small angle X-ray scattering for the study of biomolecular structure and dynamics. *Arch Biochem Biophys* **628**: 33–41. doi:10.1016/j.abb.2017.05.005
- Norris M, Fetler B, Marchant J, Johnson BA. 2016. NMRFX Processor: a cross-platform NMR data processing program. *J Biomol NMR* **65**: 205–216. doi:10.1007/s10858-016-0049-6
- Ohlenschläger O, Wöhnert J, Bucci E, Seitz S, Häfner S, Ramachandran R, Zell R, Görlach M. 2004. The structure of the stemloop D subdomain of coxsackievirus B3 cloverleaf RNA and its interaction with the proteinase 3C. *Structure* **12**: 237–248. doi:10.1016/j.str.2004.01.014
- Parisien M, Major F. 2008. The MC-Fold and MC-Sym pipeline infers RNA structure from sequence data. *Nature* **452**: 51–55. doi:10.1038/nature06684
- Parsley TB, Towner JS, Blyn LB, Ehrenfeld E, Semler BL. 1997. Poly (rC) binding protein 2 forms a ternary complex with the 5'-terminal sequences of poliovirus RNA and the viral 3CD proteinase. *RNA* **3**: 1124–1134.
- Petoukhov MV, Franke D, Shkumatov AV, Tria G, Kikhney AG, Gajda M, Gorba C, Mertens HD, Konarev PV, Svergun DI. 2012. New developments in the ATSAS program package for small-angle scattering data analysis. *J Appl Crystallogr* **45**: 342–350. doi:10.1107/S0021889812007662
- Pilipenko EV, Blinov VM, Romanova LI, Sinyakov AN, Maslova SV, Agol VI. 1989. Conserved structural domains in the 5'-untranslated region of picornaviral genomes: an analysis of the segment controlling translation and neurovirulence. *Virology* **168**: 201–209. doi:10.1016/0042-6822(89)90259-6
- Popenda M, Szachniuk M, Antczak M, Purzycka KJ, Lukasiak P, Bartol N, Blazewicz J, Adamiak RW. 2012. Automated 3D structure composition for large RNAs. *Nucleic Acids Res* **40**: e112. doi:10.1093/nar/gks339
- Rambo RP, Tainer JA. 2013. Accurate assessment of mass, models and resolution by small-angle scattering. *Nature* **496**: 477–481. doi:10.1038/nature12070
- Rivera VM, Welsh JD, Maizel JV Jr. 1988. Comparative sequence analysis of the 5' noncoding region of the enteroviruses and rhinoviruses. *Virology* **165**: 42–50. doi:10.1016/0042-6822(88)90656-3
- Schwieters CD, Kuszewski JJ, Tjandra N, Clore GM. 2003. The Xplor-NIH NMR molecular structure determination package. *J Magn Reson* **160**: 65–73. doi:10.1016/S1090-7807(02)00014-9
- Simon B, Masiewicz P, Ephrussi A, Carlomagno T. 2015. The structure of the SOLE element of oskar mRNA. *RNA* **21**: 1444–1453. doi:10.1261/ma.049601
- Svergun DI. 1992. Determination of the regularization parameter in indirect-transform methods using perceptual criteria. *J Appl Crystallogr* **25**: 495–503.
- Svergun D, Barberato C, Koch MHJ. 1995. CRYSOLE—a program to evaluate x-ray solution scattering of biological macromolecules from atomic coordinates. *J Appl Crystallogr* **28**: 768–773. doi:10.1107/S0021889895007047
- Tanaka Y, Fujii S, Hiroaki H, Sakata T, Tanaka T, Uesugi S, Tomita K, Kyogoku Y. 1999. A'-form RNA double helix in the single crystal structure of r(UGAGCUUCGGCUC). *Nucleic Acids Res* **27**: 949–955. doi:10.1093/nar/27.4.949
- Tinoco I, Bustamante C. 1999. How RNA folds. *J Mol Biol* **293**: 271–281. doi:10.1006/jmbi.1999.3001

- Warden MS, Tonelli M, Cornilescu G, Liu D, Hoppersberger LJ, Ponniah K, Pascal SM. 2017. Structure of RNA stem loop B from the picornavirus replication platform. *Biochemistry* **56**: 2549–2557. doi:10.1021/acs.biochem.7b00141
- Woodson SA. 2005. Metal ions and RNA folding: a highly charged topic with a dynamic future. *Curr Opin Chem Biol* **9**: 104–109. doi:10.1016/j.cbpa.2005.02.004
- Ying J, Wang J, Grishaev A, Yu P, Wang YX, Bax A. 2011. Measurement of ^1H - ^{15}N and ^1H - ^{13}C residual dipolar couplings in nucleic acids from TROSY intensities. *J Biomol NMR* **51**: 89–103. doi:10.1007/s10858-011-9544-y
- Zweckstetter M. 2008. NMR: prediction of molecular alignment from structure using the PALES software. *Nat Protoc* **3**: 679–690. doi:10.1038/nprot.2008.36



RNA

A PUBLICATION OF THE RNA SOCIETY

Conformational flexibility in the enterovirus RNA replication platform

Meghan S. Warden, Kai Cai, Gabriel Cornilescu, et al.

RNA 2019 25: 376-387 originally published online December 21, 2018

Access the most recent version at doi:[10.1261/rna.069476.118](https://doi.org/10.1261/rna.069476.118)

Supplemental Material

<http://rnajournal.cshlp.org/content/suppl/2018/12/21/rna.069476.118.DC1>

References

This article cites 51 articles, 15 of which can be accessed free at:
<http://rnajournal.cshlp.org/content/25/3/376.full.html#ref-list-1>

Creative Commons License

This article is distributed exclusively by the RNA Society for the first 12 months after the full-issue publication date (see <http://rnajournal.cshlp.org/site/misc/terms.xhtml>). After 12 months, it is available under a Creative Commons License (Attribution-NonCommercial 4.0 International), as described at <http://creativecommons.org/licenses/by-nc/4.0/>.

Email Alerting Service

Receive free email alerts when new articles cite this article - sign up in the box at the top right corner of the article or [click here](#).

Doing science doesn't
have to be wasteful.

USG
SCIENTIFIC

LEARN MORE

To subscribe to *RNA* go to:

<http://rnajournal.cshlp.org/subscriptions>
